Publisher's PDF, also known as Version of record

Link to published version (if available):
10.1364/OPTICA.1.000414

Link to publication record in Explore Bristol Research
PDF-document

University of Bristol - Explore Bristol Research
General rights

optica

Moving boundary and photoelastic coupling in GaAs optomechanical resonators

KRISHNA C. BALRAM,[1,2,4] MARCELO DAVANÇO,[1] JU YOUNG LIM,[3] JIN DONG SONG,[3] AND KARTIK SRINIVASAN[1,*]

[1]Center for Nanoscale Science and Technology, National Institute of Standards and Technology, Gaithersburg, Maryland 20899, USA

[2]Maryland NanoCenter, University of Maryland, College Park, Maryland 20742, USA

[3]Center for Opto-Electronic Convergence Systems, Korea Institute of Science and Technology, Seoul 136-791, South Korea

[4]e-mail: krishna.coimbatorebalram@nist.gov

*Corresponding author: kartik.srinivasan@nist.gov

Chip-based cavity optomechanical systems are being considered for applications in sensing, metrology, and quantum information science. Critical to their development is an understanding of how the optical and mechanical modes interact, quantified by the coupling rate g_0. Here, we develop GaAs optomechanical resonators and investigate the moving dielectric boundary and photoelastic contributions to g_0. First, we consider coupling between the fundamental radial breathing mechanical mode and a 1550 nm band optical whispering gallery mode in microdisks. For decreasing disk radius from $R = 5$ to $1\ \mu m$, simulations and measurements show that g_0 changes from being dominated by the moving boundary contribution to having an equal photoelastic contribution. Next, we design and demonstrate nanobeam optomechanical crystals, in which a 2.5 GHz mechanical breathing mode couples to a 1550 nm optical mode, predominantly through the photoelastic effect. We show a significant (30%) dependence of g_0 on the device's in-plane orientation, resulting from the difference in GaAs photoelastic coefficients along different crystalline axes, with fabricated devices exhibiting $g_0/2\pi$ as high as 1.1 MHz, for orientation along the [110] axis. GaAs nanobeam optomechanical crystals are a promising system, which can combine the demonstrated large optomechanical coupling strength with additional functionality, such as piezoelectric actuation and incorporation of optical gain media.   © 2014 Optical Society of America

OCIS codes: (350.4238) Nanophotonics and photonic crystals; (140.3948) Microcavity devices.

http://dx.doi.org/10.1364/OPTICA.1.000414

1. INTRODUCTION

Mechanical motion and optical fields are coupled by a number of different mechanisms in cavity optomechanical systems [1–4]. Within microscale and nanoscale geometries, perhaps the most commonly considered one is the change in effective optical path length resulting from moving dielectric boundaries, analogous to a movable mirror in a Fabry–Perot cavity. However, the optical path length also depends on the refractive index of the medium filling the cavity, and in solids this can change due to mechanical motion, because of the photoelastic (PE) effect (electrostriction) [5]. This has been observed in

stimulated Brillouin scattering, in suspended silicon waveguides [6], and cooling and excitation of traveling wave acoustic modes, in silica whispering gallery mode resonators [7,8]. More recently, it has been considered in silicon optomechanical crystals, where optimized geometries that exclusively rely on the PE effect have been developed [9].

In this paper, we investigate the moving dielectric boundary and PE contributions to the optomechanical coupling in GaAs devices. GaAs has many desirable properties for cavity optomechanics: relatively large PE coefficients [5], which can produce devices with high optomechanical coupling [9]; piezoelectric properties [10], which can be exploited for driving or readout

of mechanical motion; and potential for integration with InAs/GaAs quantum dots that offer nonclassical light emission and a strong resonant nonlinearity [11], and which can be used to probe and control mechanical motion [12,13].

We first present a combined theoretical and experimental analysis of GaAs microdisks of varying radius, where in large radius devices, the moving boundary (MB) effect dominates, while in small radius devices the photoelastic effect is the leading contribution. While these trends have recently been theoretically predicted [14], here we experimentally demonstrate the importance of considering both effects in the overall optomechanical coupling rate g_0. We then present two designs of GaAs nanobeam optomechanical crystals that rely predominantly on the PE effect. We show a significant (30%) dependence of g_0 on the in-plane device angle, in contrast with similar Si devices [9], for which the dependence is much weaker (3%). This dependence originates from the much larger magnitude and opposite sign of the PE coefficient p_{12} in GaAs. We experimentally demonstrate this effect, by measuring g_0 in devices fabricated with differing in-plane angles, and measure $g_0/2\pi$ as high as 1.1 MHz, for devices oriented along the [110] axis of GaAs. Mechanical modes at 2.5 GHz (with a quality factor $Q_m \approx 2000$ at room temperature and atmosphere) are observed, as is self-oscillation of the mechanical modes, through radiation-pressure driven dynamical back-action [15].

2. MICRODISKS

Figure 1(a) shows a scanning electron microscope image of a microdisk cavity, fabricated in a 220 nm thick GaAs layer, using typical lithography and dry etching processes (Supplement 1, Section S1). Finite-element method simulations are used to calculate the whispering gallery optical modes and radial breathing mechanical modes of such devices [Fig. 1(a)], with disk radius R varying between 1 and 5 μm. For each value of R, we calculate optical modes of transverse electric (TE) polarization (dominant

electric field components are in the plane of the disk), and determine the azimuthal mode number m, that places a first-order radial mode in the 1550 nm band. We focus on the $\mathrm{TE}_{(1,m)}$ mode, because of its comparatively high radiation-limited optical quality factor (Q_o) for small disks ($R \gtrsim 1$ μm). Similarly, we focus on the fundamental radial breathing mechanical mode, as it is expected to have a higher mechanical quality factor (Q_m) than higher-order modes, for a given supporting pedestal size.

The optomechanical coupling rate g_0, defined as the optical mode frequency shift due to the mechanical mode's zero-point motion [16], has MB ($g_{0,\mathrm{MB}}$) and PE ($g_{0,\mathrm{PE}}$) contributions obtained from the calculated modes as in [9]

$$g_{0,\mathrm{MB}} = -\frac{\omega_0}{2} \frac{\oint_A \mathrm{d}A(\mathbf{Q} \cdot \hat{\mathbf{n}})(\Delta\epsilon|\mathbf{E}_{||}|^2 - \Delta\epsilon^{-1}|\mathbf{D}_\perp|^2)}{\int \mathrm{d}V \epsilon|\mathbf{E}|^2}, \quad (1)$$

$$\begin{aligned} g_{0,\mathrm{PE}} = &-\frac{\omega_0 \epsilon_0 n^4}{2} \frac{\int \mathrm{d}V \sum(|\mathbf{E}|^2 (p_{11}S_{xx} + p_{12}(S_{yy} + S_{zz})))}{\int \mathrm{d}V \epsilon|\mathbf{E}|^2} \\ &-\frac{\omega_0 \epsilon_0 n^4}{2} \frac{\int \mathrm{d}V \sum(|\mathbf{E}|^2 4\mathrm{Re}(E_x^* E_y)p_{44}S_{xy})}{\int \mathrm{d}V \epsilon|\mathbf{E}|^2}, \end{aligned} \quad (2)$$

where $\sum$ is a summation, according to the Einstein notation $x \to y \to z \to x$. The p_{ii} are the PE coefficients of GaAs [17] ($p_{11} = -0.165$, $p_{12} = -0.14$, and $p_{44} = -0.072$), S_{ii} is the strain, and $\mathbf{Q}$ is normalized mechanical displacement with $\hat{\mathbf{n}}$ being the surface normal direction. In addition, ω_0 is the optical frequency, ϵ_0 is the permitivitty of free-space, and n is the refractive index. Qualitatively, the PE contribution is sensitive to mechanical motion throughout the device, whereas the MB contribution is sensitive to the motion of surfaces (particularly the disk sidewall for the radial breathing mode).

Figure 2 shows the calculated contribution to g_0, due to the MB (blue) and PE (green) effects, as a function of R. For $R \gtrsim 1.25$ μm, the MB effect dominates, whereas for
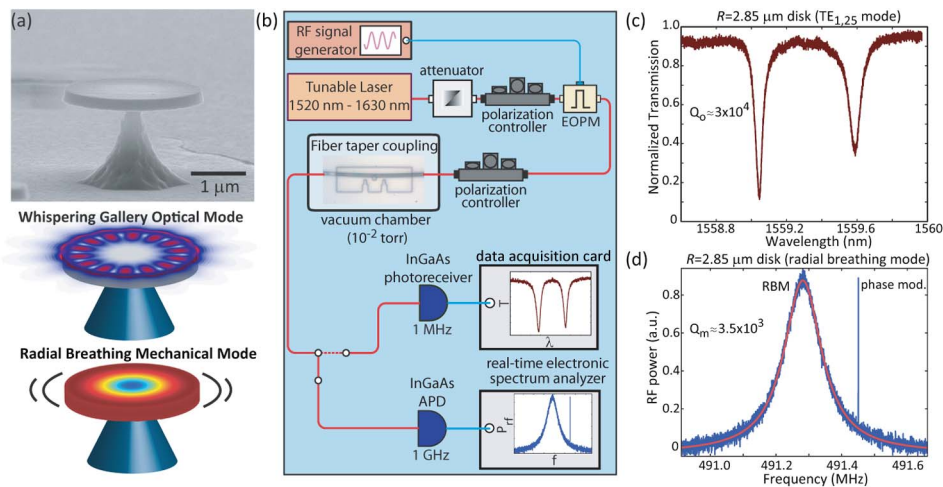

Fig. 1. GaAs microdisk optomechanical resonators; (a) scanning electron microscope image of a fabricated device, and finite-element method simulations of the optical ($\mathrm{TE}_{1,7}$) and mechanical mode (1.4 GHz radial breathing mode), in a $R = 1$ μm microdisk; (b) experimental setup for measuring the optomechanical coupling; APD, avalanche photodiode; EOPM, electrooptic phase modulator; (c) optical transmission spectrum for the $\mathrm{TE}_{1,25}$ mode, in a $R = 2.85$ μm radius device; (d) thermal noise spectrum for the ≈490 MHz radial breathing mode, shown together with the Lorentzian fit (red), and the phase modulator calibration peak.
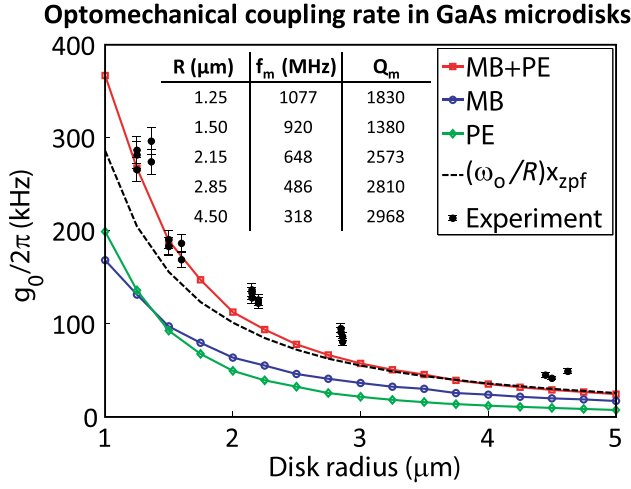
Fig. 2. Optomechanical coupling rate g_0, as a function of radius R, for coupling between the $TE_{1,m}$ optical modes and fundamental radial breathing mechanical modes. Red, blue, and green curves are the calculated total coupling rate (MB + PE), MB contribution, and PE contribution, respectively. Dashed black line is a rough estimate $g_0 = (\omega_o/R)x_{zpf}$, where ω_o is the optical frequency, and x_{zpf} is the zero-point motion amplitude. Black circles are experimental values, where the error bars are dominated by uncertainty in the modulator V_π, and are 1 standard deviation values. Inset gives the measured mechanical frequency and Q_m.

$R \lesssim 1.25$ µm, the PE effect is comparable, or even slightly larger. This is consistent with recent simulation results for similar GaAs microdisks [14]. To verify this scaling behavior experimentally [Fig. 1(b)], we measure fabricated GaAs microdisks of varying radius, following an approach similar to [16], where a calibration signal of known modulation index β_{pm}, from a phase modulator driven close to the mechanical resonance frequency, is used to determine the magnitude of g_0 (Supplement 1, Section S3). Figures 1(c)–1(d) show representative optical and mechanical modes for a device, where the mechanical mode spectrum also includes the phase modulator calibration tone. Compared to microdisks fabricated previously, using an essentially identical process [18], Q_o in these devices ($<5 \times 10^4$) is an order of magnitude lower, likely as a result of 100 nm length scale roughness present on the underside of the GaAs layer (Supplement 1, Section S2). Such lower Q_o values do not influence the estimate of g_0, but do prevent operation in the sideband-resolved regime, needed for a number of applications.

The optomechanical coupling rate g_0 can be estimated from a mechanical mode spectrum as (Supplement 1, Section S3)

$$g_0^2 = \frac{\hbar \Omega_m}{2k_B T} \Omega_m^2 \beta_{pm}^2 \frac{S_{cav}(\Omega_m)}{S_{pm}(\Omega_{mod})}, \qquad (3)$$

where $S_{cav}(\Omega_m)$ is the power in the mechanical mode, $S_{pm}(\Omega_{mod})$ is the power in the phase modulator signal, and β_{pm} is the modulation index. $\beta_{pm} = \pi \frac{V_{sig}}{V_\pi}$, where V_{sig} is the applied voltage, and V_π (the voltage required to produce a π phase shift) is determined through a separate calibration (Supplement 1, Section S4).

The experimentally measured g_0 values, for disks of varying R, are plotted in Fig. 2 (black circles), where the uncertainty in each measurement is dominated by the uncertainty in the phase modulator V_π. The data shows good agreement with the red curve, which plots the sum of the MB and the PE contributions to g_0. Especially for small disk radii, the data shows significant deviation from the MB contribution alone, which might help explain some discrepancies observed in previous measurements of GaAs disk optomechanical resonators, where only MB effects were considered in simulation comparisons [19]. We note that for nominally identical disks, a spread in g_0 of ≈10% is observed. We attribute this to the specifics of the fiber taper coupling for each device which, we have observed, can perturb the optical and mechanical modes, and the resultant optomechanical coupling (Supplement 1, Section S5).

3. NANOBEAM OPTOMECHANICAL CRYSTALS

The measurements of g_0 in GaAs microdisks demonstrated that the contribution due to the PE effect ($g_{0,PE}$) can become comparable to (and even exceed that due to) the MB effect ($g_{0,MB}$), as the disk radius R becomes comparable to the wavelength. Intuitively, as R is reduced, the volume of both the optical and mechanical modes decrease, and g_0 increases, due to increased spatial overlap. Given that bending loss starts to dominate Q_o, for $R < 0.7$ µm, one can estimate that $g_0/2\pi \lesssim 450$ kHz, based on the data shown in Fig. 2. For higher g_0, one needs to consider geometries that support more tightly confined optical and mechanical modes.

Optomechanical crystals [20], structures that spatially co-localize optical modes within a photonic bandgap and mechanical modes within a phononic bandgap, have been demonstrated in a number of materials [9,21–25], and in both one- and two-dimensional geometries. Here, we focus on one-dimensional nanobeam geometries, where the nanobeams are patterned with a series of holes, whose dimensions are graded quadratically from the center (cavity section) to the edge (mirror section). The general design principle for the optical cavity [26] relies on choosing the center hole dimension to support a guided mode, and then quadratically tapering the hole dimension down to the mirror section, where the mode lies in the forbidden band, and hence is reflected. The cavity is constructed by putting two such tapers back-to-back. The quadratic taper ensures that the electric field amplitude of the mode has a Gaussian profile, and retains high Q_o. Similar design concepts have been used in the development of GaAs nanobeam photonic crystal cavities, for applications in lasing [27] and cavity quantum electrodynamics [28]. Here, we demonstrate these GaAs cavities in the context of cavity optomechanics, where we note that the tailoring of the hole dimensions also enables localization of mechanical modes [20].

Figure 3 shows two different nanobeam optomechanical crystal cavity designs, in 220 nm thick GaAs, using circular holes [Figs. 3(a)–3(d)], as described previously, and elliptical holes [Figs. 3(e)–3(h)], in an approach similar to [9]. For each design, we show a schematic of the geometry, the variation in device parameters (as a function of hole number), and the optical and mechanical modes. We designed the devices to have a
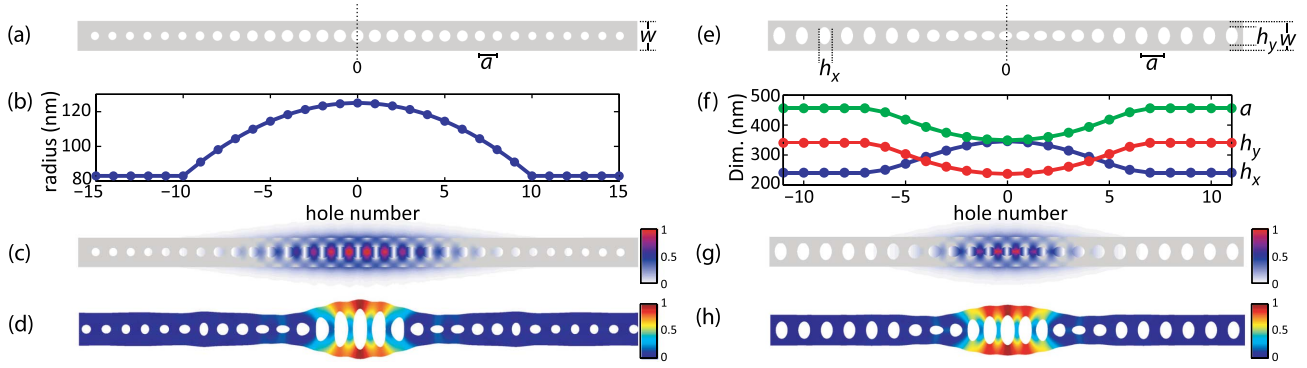
Fig. 3. GaAs nanobeam optomechanical crystal designs, with (a)–(d) showing results for a circular hole geometry and (e)–(h) showing results for an elliptical hole geometry. (a) Circular hole geometry design; (b) circular hole geometry variation in design parameters as a function of hole number; (c) circular hole geometry normalized electric field amplitude; (d) circular hole geometry normalized mechanical displacement; (e) elliptical hole geometry design; (f) elliptical hole geometry variation in design parameters as a function of hole number; (g) elliptical hole geometry normalized electric field amplitude; and (h) elliptical hole geometry normalized mechanical displacement.

nominal operating wavelength of 1550 nm, and ran a parameter sweep to find designs with the highest $g_0 Q_o$, where both MB and PE contributions to g_0 are calculated, as described previously for microdisks.

The circular hole design is one realization of the more general elliptical hole design, and is thus comparatively simple, in terms of the number of design parameters. In particular, we fix the lattice constant a, and adjust only the hole radius r at the different lattice sites. More specifically, we vary the hole radius in the center of the cavity and the mirror sections, as well as the steepness of the quadratic grading profile (i.e., the number of holes over which the radius is tapered). In comparison, the elliptical hole designs have quadratic grades for the lattice constant (a) and lengths of the principal axes of the ellipse (h_x and h_y). Thus, for each dimension a, h_x, and h_y, we vary the value in the center of the cavity and the mirror sections, as well as the steepness of the quadratic grade.

While for both the circular and elliptical hole designs, we find parameters for which $Q_o > 10^6$, g_0 is higher for the elliptical hole designs. In particular, the optimized elliptical hole design has $g_{0,PE}/2\pi = 860$ kHz and $g_{0,MB}/2\pi = -94$ kHz, for coupling between the $\lambda \approx 1535$ nm optical mode and $\Omega_m/2\pi \approx 2.14$ GHz mechanical mode, compared to the optimized circular hole design, with $g_{0,PE}/2\pi = 563$ kHz and $g_{0,MB}/2\pi = -43$ kHz, for coupling between the $\lambda \approx 1545$ nm optical mode and $\Omega_m/2\pi \approx 2.31$ GHz mechanical mode. The elliptical design ensures a higher g_0 by having a higher GaAs volume fraction in the center of the beam. We note that while in microdisks, the MB and PE contributions to g_0 are comparable in magnitude, and of the same sign, for the optimized nanobeams, g_0 is dominated by the PE effect, and the MB contribution is opposite in sign, and thus reduces the net optomechanical coupling rate. This behavior is consistent with [9,24], where an optimized nanobeam geometry, dominated by the PE effect, was developed for Si [9] and diamond [24].

Given that the PE effect is represented by a tensor, one would expect the contribution to g_0 to depend on the in-plane orientation of the nanobeam. Moreover, the fact that p_{12} has a much larger magnitude in GaAs than in Si

($p_{12,GaAs} = -0.14$, $p_{12,Si} = 0.017$) suggests that the dependence of g_0 on in-plane orientation will be much more significant in GaAs. Figure 4(b) shows $g_{0,PE}$ for the elliptical hole nanobeam, shown in Figs. 3(e)–3(h), as a function of the angle the long axis of the nanobeam makes with the [100] direction. Here, the coupling rate is calculated using the rotated PE tensor (Supplement 1, Section S8), and an isotropic elastic tensor is used for both GaAs and Si. As we discuss subsequently in the text, using the full anisotropic elastic tensor [29,30] leads to corrections in both the MB and PE coupling rates, although the total g_0 values are within 10% of the values calculated with the isotropic elastic tensor.

We can see from Fig. 4(b) that the effect of in-plane orientation on g_0 is quite significant, with a variation of almost 35%, and a peak value $g_{0,PE}/2\pi \approx 1.2$ MHz at 45° (device orientation along [110]). We also plot the orientation dependence of $g_{0,PE}$ for a silicon nanobeam optomechanical crystal, similar to that of [9] (Supplement 1, Section S7). We see that again there is a dependence of $g_{0,PE}$ on in-plane orientation, although in this case, the optomechanical coupling rate is minimized at 45°, and the variation between 0° and 45° is less than 5%. To understand this, we plot in Fig. 4(c) the contributions due to the ($p_{11} + p_{44}$) and p_{12} terms of Eq. (2), as a function of in-plane angle. The in-plane anisotropy of $g_{0,PE}$ is seen to arise primarily from the contribution due to the p_{12} term, and the previously mentioned difference in the p_{12} values for GaAs and Si helps us understand why this rotational dependence is so weak in Si. The MB contribution $g_{0,MB}$ is insensitive to in-plane orientation, under the assumption of GaAs being an isotropic elastic material [as can be seen from the form of Eq. (1)]. The total optomechanical coupling rate for the GaAs elliptical hole design, including both PE and MB contributions, is therefore as high as $g_0/2\pi \approx 1.1$ MHz.

We study this orientation-dependent optomechanical coupling by fabricating a series of GaAs nanobeam devices, according to the elliptical hole geometry described previously, while varying the orientation of the long axis of the nanobeam, between [110] and [100], as shown in Fig. 5(a). Devices are tested in the same measurement setup used to test the microdisk samples [Fig. 1(b)]. In this case, the sample is kept
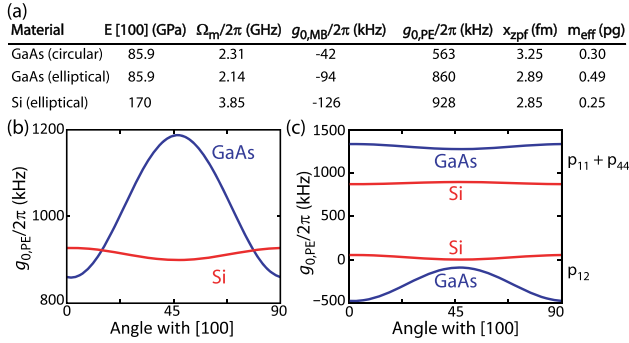
(a)

Material	E [100] (GPa)	$\Omega_m/2\pi$ (GHz)	$g_{0,MB}/2\pi$ (kHz)	$g_{0,PE}/2\pi$ (kHz)	x_{zpf} (fm)	m_{eff} (pg)
GaAs (circular)	85.9	2.31	-42	563	3.25	0.30
GaAs (elliptical)	85.9	2.14	-94	860	2.89	0.49
Si (elliptical)	170	3.85	-126	928	2.85	0.25

Fig. 4. (a) Parameters for GaAs and Si nanobeam optomechanical crystal designs, including Young's modulus along [100], mechanical mode frequency, optical wavelength, $g_{0,MB}$, $g_{0,PE}$ (nanobeam long axis oriented along the [100] direction), zero-point motional amplitude, and effective motional mass; (b) dependence of $g_{0,PE}$ for the GaAs and Si elliptical designs on in-plane rotational angle; (c) breakdown of $g_{0,PE}$, into $p_{11} + p_{44}$ (top) and p_{12} (bottom) terms.

at atmospheric pressure, as gas damping is expected to have limited influence on the mechanical modes, due to their high frequencies [31], an effect that has also been observed recently in Si_3N_4 nanobeam optomechanical crystals [23]. Optical modes in the 1550 nm band are observed with typical quality factors $Q_o \approx 4.0 \times 10^4$ [Figs. 5(b) and 5(c)]. Mechanical quality factors are typically around $Q_m \approx 2 \times 10^3$.

Using the phase modulator calibration approach described in Section 2, we extract the optomechanical coupling rate for the different devices, with $g_0/2\pi = 870$ kHz ± 45 kHz for the device aligned along [100] [Fig. 5(c)], and $g_0/2\pi = 1.12$ MHz ± 0.06 MHz for the device aligned along [110] [Fig. 5(b)]. These values correspond reasonably well with simulations, which when taking into account both the PE [Fig. 4(b)] and MB [Fig. 4(a)] contributions, predict $g_0/2\pi = 770$ kHz and $g_0/2\pi = 1.09$ MHz, respectively. Measurement of devices fabricated at an intermediate angle of 15° with respect to [100] (not shown) yield $g_0/2\pi = 920$ kHz ± 50 kHz, which also matches reasonably well with the simulation result of $g_0/2\pi = 850$ kHz. We note that while the uncertainty values we have quoted for the measured g_0 are the 1 standard deviation value due to the uncertainty in the phase modulator V_π, another source of uncertainty is in the precise angle with which the cavity was fabricated relative to the GaAs crystal planes (i.e., the alignment of the GaAs chip within the electron-beam lithography system). In particular, for intermediate device orientation angles, between [100] and [110], Fig. 4(b) predicts a variation in $g_0/2\pi$ of ≈ 50 kHz for a 5° offset in orientation.

While our experimental results are in reasonable agreement with the simulations presented thus far, one potential source of discrepancy is the use of an isotropic elastic tensor in the calculations. The anisotropy of GaAs leads to an orientation-dependent Young's modulus, Poisson's ratio, and shear modulus. One consequence of this is an orientation-dependent mechanical mode frequency, with devices oriented along [110] expected to have a frequency that is ≈ 100 MHz higher than devices oriented along [100], resulting primarily from the
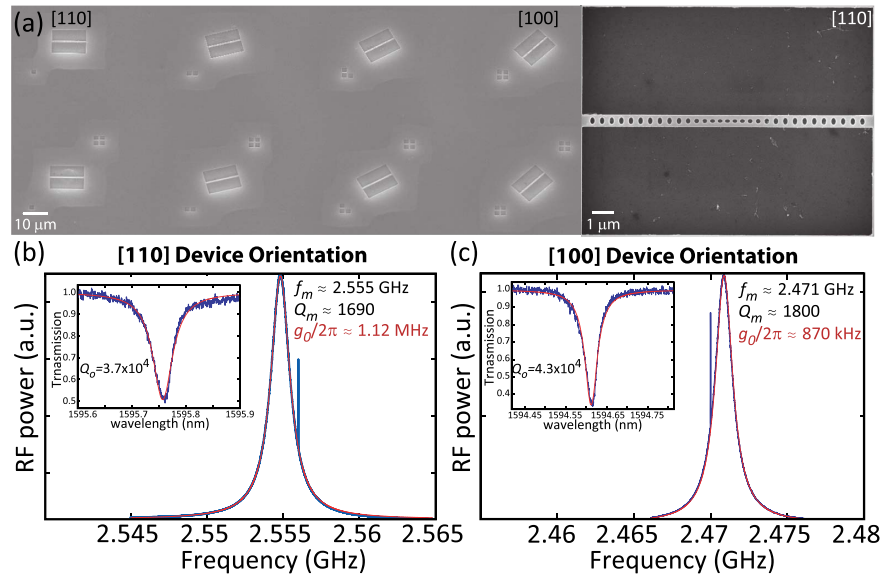

Fig. 5. GaAs nanobeam optomechanical crystal measurements; (a) scanning electron microscope image of an array of fabricated devices, where the orientation of the nanobeam long axis is varied between [110] and [100]. Right image is zoomed-in on a single nanobeam cavity, aligned along the [110] axis; (b) thermal noise spectrum (blue curve) and Lorentzian fit (red curve), for a nanobeam breathing mode, when the device is aligned along the [110] axis. The phase modulator calibration approach is used to extract the optomechanical coupling rate $g_0/2\pi = 1.12$ MHz ± 0.06 MHz. Inset shows the transmission spectrum (blue) and fit (red) for the nanobeam optical mode; (c) thermal noise spectrum (blue curve) and Lorentzian fit (red curve), for a nanobeam breathing mode, when the device is aligned along the [100] axis. The phase modulator calibration approach is used to extract the optomechanical coupling rate $g_0/2\pi = 870$ kHz ± 45 kHz. Inset shows the transmission spectrum (blue) and fit (red) for the nanobeam optical mode. Uncertainty values in g_0 are dominated by uncertainty in the modulator V_π, and are 1 standard deviation values.
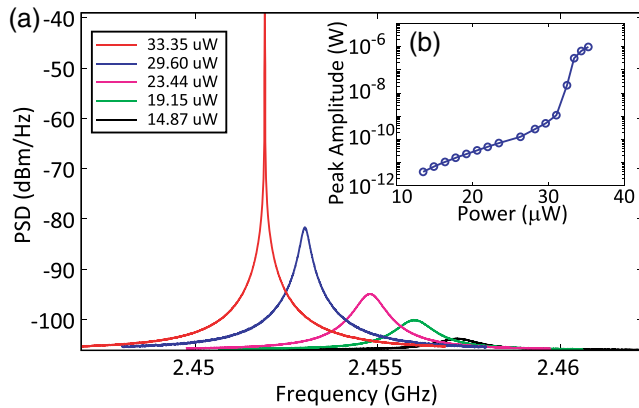
Fig. 6. (a) Mechanical mode spectra, as a function of increasing optical power injected into a GaAs nanobeam optomechanical crystal, aligned along the [100] axis, showing a pronounced linewidth narrowing and peak height increase; (b) mechanical mode peak amplitude as a function of injected optical power, showing a clear threshold behavior, indicative of the system being driven into regenerative mechanical oscillation. Uncertainty in the peak amplitude is less than the data point size.

anisotropy in the Young's modulus (Supplement 1, Section S9). This corresponds well with the experiments, where a shift of ≈85 MHz was measured for the corresponding devices.

In addition, the precise displacement profile of the mechanical mode will change (Supplement 1, Section S10). This in turn causes a change in both the MB and PE coupling rates, with the former no longer orientation-independent, as was previously assumed. Using the full anisotropic tensor, we calculate $g_{0,MB}/2\pi = -73$ kHz and $g_{0,PE}/2\pi = 923$ kHz along [100], and $g_{0,MB}/2\pi = -15$ kHz and $g_{0,PE}/2\pi = 1.07$ MHz, along [110]. The total $g_0/2\pi$, along [100] ($g_0/2\pi = 850$ kHz) and [110] ($g_0/2\pi = 1.06$ MHz), are within 10% of the values reported in Fig. 4, on account of being dominated by the PE effect. We note that the g_0 values calculated using the anisotropic elastic tensor for GaAs show closer agreement with our experimental results than the results shown in Fig. 4, where GaAs was treated as an isotropic elastic material.

Finally, by injecting increasing levels of optical power into the devices, while keeping the laser frequency blue-detuned and on the shoulder of the optical cavity mode, we can drive the system into regenerative mechanical oscillation [15]. Figure 6(a) shows a series of mechanical mode spectra for a device oriented along [100], as a function of increasing optical power, from which a clear linewidth narrowing (and peak amplitude increase) are observed. The peak amplitude is plotted as a function of input optical power in Fig. 6(b). Here, a characteristic threshold behavior at an input power <35 μW is seen, indicating that the system is indeed self-oscillating.

4. CONCLUSIONS

In summary, we have compared the moving dielectric boundary and photoelastic contributions to the optomechanical coupling rate in GaAs optomechanical resonators. Simulations and experiments in microdisk cavities correspond closely, and show that these two effects have near equal magnitude for

devices with a radius near 1 μm. Simulations and experiments on nanobeam optomechanical crystals, optimized for PE coupling (1 order of magnitude larger than the MB effect), show a significant dependence on the in-plane orientation of the nanobeam, with overall coupling rates $g_0/2\pi = 1.1$ MHz achieved for coupling between 1550 nm optical modes and 2.5 GHz mechanical modes. Along with recent works exploiting the PE effect in silicon-based devices [6,9], our results indicate the importance of considering the effect in the development of cavity optomechanical devices. Moreover, the anisotropy of both the PE and elastic tensors indicates that device orientation must be taken into account during layout. Finally, while our experimental results are consistent with simulations based on the values of the PE coefficients found in the literature, in general, there is a limited amount of data available on this topic, particularly as a function of wavelength, and in different material systems. Such measurements would be extremely valuable for the continued development of optomechanical platforms, especially as they move toward higher mechanical frequencies involving acoustic wave resonances.

REFERENCES

1. M. Aspelmeyer, T. J. Kippenberg, and F. Marquardt, "Cavity optomechanics," arXiv:1303.0733 (2013).
2. I. Favero and K. Karrai, "Optomechanics of deformable optical cavities," Nat. Photonics **3**, 201–205 (2009).
3. M. Li, W. H. P. Pernice, and H. X. Tang, "Reactive cavity optical force on microdisk-coupled nanomechanical beam waveguides," Phys. Rev. Lett. **103**, 223901 (2009).
4. M. Wu, A. C. Hryciw, C. Healey, D. P. Lake, H. Jayakumar, M. R. Freeman, J. P. Davis, and P. E. Barclay, "Dissipative and dispersive optomechanics in a nanocavity torque sensor," Phys. Rev. X **4**, 021052 (2014).
5. P. T. Rakich, P. Davids, and Z. Wang, "Tailoring optical forces in waveguides through radiation pressure and electrostrictive forces," Opt. Express **18**, 14439–14453 (2010).
6. H. Shin, W. Qiu, R. Jarecki, J. A. Cox, R. H. Olsson, A. Starbuck, Z. Wang, and P. T. Rakich, "Tailorable stimulated Brillouin scattering in nanoscale silicon waveguides," Nat. Commun. **4**, 1944 (2013).
7. G. Bahl, J. Zehnpfennig, M. Tomes, and T. Carmon, "Stimulated optomechanical excitation of surface acoustic waves in a microdevice," Nat. Commun. **2**, 403 (2011).
8. G. Bahl, M. Tomes, F. Marquardt, and T. Carmon, "Observation of spontaneous Brillouin cooling," Nat. Phys. **8**, 203–207 (2012).

9. J. Chan, A. H. Safavi-Naeini, J. T. Hill, S. Meenehan, and O. Painter, "Optimized optomechanical crystal cavity with acoustic radiation shield," Appl. Phys. Lett. **101**, 081115 (2012).

10. S. C. Masmanidis, R. B. Karabalin, I. De Vlaminck, G. Borghs, M. R. Freeman, and M. L. Roukes, "Multifunctional nanomechanical systems via tunably coupled piezoelectric actuation," Science **317**, 780–783 (2007).

11. P. Michler, ed., *Single Semiconductor Quantum Dots* (Springer, 2009).

12. I. Wilson-Rae, P. Zoller, and A. Imamoğlu, "Laser cooling of a nanomechanical resonator mode to its quantum ground state," Phys. Rev. Lett. **92**, 075507 (2004).

13. I. Yeo, P.-L. de Assis, A. Gloppe, E. Dupont-Ferrier, P. Verlot, N. S. Malik, E. Dupuy, J. Claudon, J.-M. Gérard, A. Auffèves, G. Nogues, S. Seidelin, J.-P. Poizat, O. Arcizet, and M. Richard, "Strain-mediated coupling in a quantum dot-mechanical oscillator hybrid system," Nat. Nanotechnol. **9**, 106–110 (2014).

14. C. Baker, W. Hease, D.-T. Nguyen, A. Andronico, S. Ducci, G. Leo, and I. Favero, "Photoelastic coupling in gallium arsenide optomechanical disk resonators," Opt. Express **22**, 14072–14086 (2014).

15. T. J. Kippenberg and K. J. Vahala, "Cavity opto-mechanics," Opt. Express **15**, 17172–17205 (2007).

16. M. L. Gorodetsky, A. Schliesser, G. Anetsberger, S. Deleglise, and T. J. Kippenberg, "Determination of the vacuum optomechanical coupling rate using frequency noise calibration," Opt. Express **18**, 23236–23246 (2010).

17. R. W. Dixon, "Photoelastic properties of selected materials and their relevance for applications to acoustic light modulators and scanners," J. Appl. Phys. **38**, 5149–5153 (1967).

18. K. Srinivasan, M. Borselli, T. J. Johnson, P. E. Barclay, O. Painter, A. Stintz, and S. Krishna, "Optical loss and lasing characteristics of high-quality-factor AlGaAs microdisk resonators with embedded quantum dots," Appl. Phys. Lett. **86**, 151106 (2005).

19. L. Ding, C. Baker, P. Senellart, A. Lemaitre, S. Ducci, G. Leo, and I. Favero, "High frequency GaAs nano-optomechanical disk resonator," Phys. Rev. Lett. **105**, 263903 (2010).

20. M. Eichenfield, J. Chan, R. M. Camacho, K. J. Vahala, and O. Painter, "Optomechanical crystals," Nature **462**, 78–82 (2009).

21. L. Fan, X. Sun, C. Xiong, C. Schuck, and H. X. Tang, "Aluminum nitride piezo-acousto-photonic crystal nanocavity with high quality factors," Appl. Phys. Lett. **102**, 153507 (2013).

22. J. Bochmann, A. Vainsencher, D. D. Awschalom, and A. N. Cleland, "Nanomechanical coupling between microwave and optical photons," Nat. Phys. **9**, 712–716 (2013).

23. M. Davanço, S. Ates, Y. Liu, and K. Srinivasan, "Si$_3$N$_4$ optomechanical crystals in the resolved-sideband regime," Appl. Phys. Lett. **104**, 041101 (2014).

24. L. Kipfstuhl, F. Guldner, J. Riedrich-Möller, and C. Becher, "Modeling of optomechanical coupling in a phoxonic crystal cavity in diamond," Opt. Express **22**, 12410–12423 (2014).

25. Q. Rolland, M. Oudich, S. El-Jallal, S. Dupont, Y. Pennec, J. Gazalet, J. Kastelik, G. Leveque, and B. Djafari-Rouhani, "Acousto-optic couplings in two-dimensional phoxonic crystal cavities," Appl. Phys. Lett. **101**, 061109 (2012).

26. Q. Quan and M. Loncar, "Deterministic design of wavelength scale, ultra-high Q photonic crystal nanobeam cavities," Opt. Express **19**, 18529–18542 (2011).

27. Y. Gong, B. Ellis, G. Shambat, T. Sarmiento, J. S. Harris, and J. Vuckovic, "Nanobeam photonic crystal cavity quantum dot laser," Opt. Express **18**, 8781–8789 (2010).

28. R. Ohta, Y. Ota, M. Nomura, N. Kumagai, S. Ishida, S. Iwamoto, and Y. Arakawa, "Strong coupling between a photonic crystal nanobeam cavity and a single quantum dot," Appl. Phys. Lett. **98**, 173104 (2011).

29. W. Brantley, "Calculated elastic constants for stress problems associated with semiconductor devices," J. Appl. Phys. **44**, 534–535 (1973).

30. M. A. Hopcroft, W. D. Nix, and T. W. Kenny, "What is the Young's modulus of silicon?" J. Microelectromech. Syst. **19**, 229–238 (2010).

31. D. M. Karabacak, V. Yakhot, and K. L. Ekinci, "High-frequency nanofluidics: an experimental study using nanomechanical resonators," Phys. Rev. Lett. **98**, 254505 (2007).